Determination of Maximum Turbulent Energy Dissipation Rate generated by a Rushton Impeller through Large Eddy Simulation

Miroslav Soos
Institute for Chemical and Bioengineering, Dept. of Chemistry and Applied Biosciences, ETH Zurich, 8093 Zurich, Switzerland

René Kaufmann and Raphael Winteler
Institute of Environmental Engineering, ETH Zurich, CH 8093 Zurich, Switzerland

Martin Kroupa
Institute for Chemical and Bioengineering, Dept. of Chemistry and Applied Biosciences, ETH Zurich, 8093 Zurich, Switzerland

Beat Lüthi
Institute of Environmental Engineering, ETH Zurich, CH 8093 Zurich, Switzerland

photrack AG, Am Wasser 148, 8049 Zurich, Switzerland

DOI 10.1002/aic.14206
Published online August 23, 2013 in Wiley Online Library (wileyonlinelibrary.com)

Large eddy simulation (LES) of a stirred tank equipped with a Rushton impeller and four cylindrical baffles was used to characterize the flow pattern and to assess the maximum turbulent kinetic energy dissipation rate ε_{max}. While the shorter baffle-impeller distance significantly affects the radial velocity profile and the trailing vortices expansion, the flow field in the impeller vicinity is comparable to that of a standard setup with rectangular baffles connected to the wall. The phase-resolved profile of ε_{max} indicates its very strong variation from $10 \cdot N^3 D^2$ to $130 \pm 13 \cdot N^3 D^2$. When using peak values of the corresponding hydrodynamic stress $\tau_{max}\left(=\sqrt{\mu\rho\varepsilon_{max}}\right)$, the maximum stable aggregate size measured in the same stirred tank closely correlates with breakage data obtained under laminar conditions using the same initial aggregates. This indicates that the same mechanism was involved in the aggregate breakup under both conditions, allowing us to predict aggregates breakup under various conditions. © 2013 American Institute of Chemical Engineers
AIChE J, 59: 3642–3658, 2013
Keywords: large eddy simulation, stirred tank, rushton turbine, turbulent flow, energy dissipation rate, aggregate breakup

Introduction

Coagulation or flocculation is commonly used to enlarge the characteristic size of dispersed colloidal particles which facilitates their efficient separation.[1] On addition of proper amount of coagulant (e.g., a salt or an acid) particles start to aggregate and form larger clusters. However, when they grow large enough the hydrodynamic stress exerted by the fluid flow increases and eventually overcomes the aggregate strength which results in aggregate breakage. The breakage rate of this process is given by the frequency of the local hydrodynamic stress exceeding a critical value required to break an aggregate.[2,3] This critical stress is identified to be the aggregate strength which is defined as the maximum hydrodynamic stress an isolated aggregate can withstand. Therefore, the quantification of the breakage behavior of aggregates under various flow conditions is of fundamental as well as practical importance when considering the design and the optimization of coagulation processes.

Several studies are available in the literature dealing with aggregate breakup using either laminar[4–9] or turbulent conditions.[10–20] In parallel to the experimental activity, mathematical modeling or theoretical considerations have been used to describe the breakup of aggregates.[2,3,9,21–28] The result of these studies is a scaling of the maximum stable size of formed aggregates as a function of the applied stress, or corresponding shear rate or energy dissipation rate ε. The critical stress can be precisely evaluated in uniform flow fields under laminar conditions, e.g., couette flow or contracting

Additional Supporting Information may be found in the online version of this article.

Current address for M. Kroupa: Dept. of Chemical Engineering, Institute of Chemical Technology, Technika 5, 166 28 Prague, Czech Republic.

Correspondence concerning this article should be addressed to M. Soos at miroslav.soos@chem.ethz.ch.

nozzle. However, under turbulent conditions the flow field is highly nonuniform resulting in unknown values of the applied stress at the breakage point. Due to this complication the breakage data are commonly plotted against the volume-averaged values even though these could be substantially different compare to those causing aggregate breakup. This clearly limits our capability to model the aggregate breakup under industrially relevant conditions.

Several techniques, such as laser Doppler anemometry (LDA),[29–32] particle image velocimetry (PIV),[31,33–35] and laser-induced fluorescence (LIF)[36] have been used to characterize the flow field generated by various impellers mounted in stirred tanks. Due to optical inaccessibility they have been mostly applied to characterize the flow field in the impeller discharge stream generated by various impellers resulting in detailed maps of the energy dissipation rate in this region of the stirred tank. In the case of Rushton impeller and stirred tank of standard geometry equipped with rectangular baffles attached to the wall, applying various spatial resolutions values of $\varepsilon_{max}/\langle\varepsilon\rangle$ cover a range from 10 to 50[32,34,37–39] have been reported. However, even higher values of ε could be present near the impeller blades and they could be underestimated using the aforementioned techniques. In fact, as shown by Wichterle et al.[40] substantially higher values of the ratio $\varepsilon_{max}/\langle\varepsilon\rangle$ in the range from 150 to 400, determined on the surface of rotating impeller blades, were found when using an indirect method based on the measurement of a diffusion controlled current from an electrolyte solution toward small electrodes located at the impeller surface.

In parallel to the experimental characterization computational modeling represents an alternative route to resolve in great details the flow in stirred tanks. Due to the high Reynolds numbers, commonly used in these devices, the two approaches Reynolds-averaged Navier-Stokes equations (RANS)[41] or large eddy simulation (LES)[31,41–56] were employed. The first approach relies on certain turbulent models to describe the turbulence inside the vessel of interest. LES is based on the idea that only the large-scale flow field is geometry dependent, and therefore, it has to be modeled directly. The small-scale turbulence, however, is assumed to behave universal,[57] and therefore, turbulence models are applied to estimate the so-called subgrid stresses. Typically, the Smagorinsky model and its further modification by Lilly[58,59] is commonly used in the LES simulations. Recently, it was shown by several authors[31,41,42,45,51,53,54] that application of LES can provide more detailed and more accurate information about turbulent quantities inside stirred tanks, e.g., kinetic energy, dissipation rate, position of trailing vortices, information about turbulence anisotropy, as compared to the RANS approach. When considering ε_{max} values of $\varepsilon_{max}/\langle\varepsilon\rangle$ in the impeller proximity covering range from about 100 up to 370 have been documented.[31,42,51]

To address the aforementioned uncertainty to determine the hydrodynamic stress responsible for the breakup of aggregates under turbulent conditions, LES combined with Smagoringky subgrid scale turbulent model was used to characterize the flow field in the stirred tank used previously for breakup experiments.[18] The obtained values of ε_{max} were used to estimate the maximum hydrodynamic stresses $\tau_{max}\left(=\sqrt{\mu\rho\varepsilon_{max}}\right)$, to which aggregates would be exposed to. These values were subsequently used to scale maximum stable aggregates sizes measured at the end of breakage experiments using a stirred tank and compared with those obtained from contracting nozzles using the same initial aggregates.[8] It was found that both laminar and turbulent data become consistent when values of τ_{max} were used for normalization. This supports the hypothesis that independent on the device type or the flow complexity, the breakup of aggregates is controlled by the same mechanism and the maximum stable aggregate size follows the same scaling independent whether the flow is laminar or turbulent.

Experimental Setup

Two sets of previously published maximum stable aggregate sizes are used in this study. The first set was measured at the end of breakage experiments using turbulent flow conditions in a stirred tank equipped with a Rushton impeller and four cylindrical baffles.[18] The second set was obtained under laminar conditions using a contracting nozzle flow.[8] Briefly, in both these experiments aggregates composed of polystyrene primary particles with diameter of 810 nm purchased from Interfacial Dynamics Corp. (IDC), Portland, OR (USA) (Product-No: 1–800, Cumulative variation = 2%, Batch No: 642,4, solid% = 8.1) were used. Preparation of the aggregates for breakage experiment was done in a 2.5 L stirred tank (for details see Figure 1a, b) applying stirring speed of 200 rpm and a solid volume fraction equal to 4.10^{-5}. To initiate the aggregation process $Al(NO_3)_3$ was added to the dispersion of stable primary particles. Aggregates sizes along the aggregation process were monitored online by light scattering instrument Mastersizer 2000 device (Malvern, U.K.). After reaching a steady-state size with an average radius of gyration around 22 microns, two different breakage experiments were performed. In the first experiment samples of aggregates were gently withdrawn from the stirred tank, diluted with a poly-vinyl alcohol solution to prevent further aggregation and consequently broken in an extensional flow generated in a contracting nozzle placed between two syringes until maximum steady state aggregate size was reached.[8] In the second approach the breakage experiment started from preformed aggregates, which were diluted in a stirred tank with a particle free salt solution until maximum stable aggregates size was reached.[18,60,61] In both these approaches the maximum stable aggregates size was measured for different flow conditions.

Due to the large size of primary particles, which is well outside the region of the validity of the Rayleigh-Debye-Gans (RDG) theory,[62,63] and due to the compact structure of the initial aggregates,[18] the variation of fragmented internal structure was evaluated from the analysis of 2-D confocal laser-scanning microscopy (CLSM) pictures. The projected surface area A, of imaged aggregates is plotted against the corresponding aggregate perimeter P. An example of such scaling obtained for initial aggregates as well as for fragments measured at the end of breakage experiments in stirred tank and in contracting nozzle is presented in Figure 2. As it can be seen initial aggregates as well those obtained after breakage experiments follow the same scaling. This is indicating that no restructuring is present during the process of aggregate breakup. In fact all aggregates can be characterized by the same perimeter fractal dimension d_{pf}[18,64,65] which in this particular case was equal to 1.14 (see Figure 2). Having determined d_{pf} the mass fractal dimension d_f was subsequently estimated using a correlation developed by Ehrl et al.,[66] which for this particular case was equal to 2.7, indicating very compact aggregates. Similarly to the d_f also the

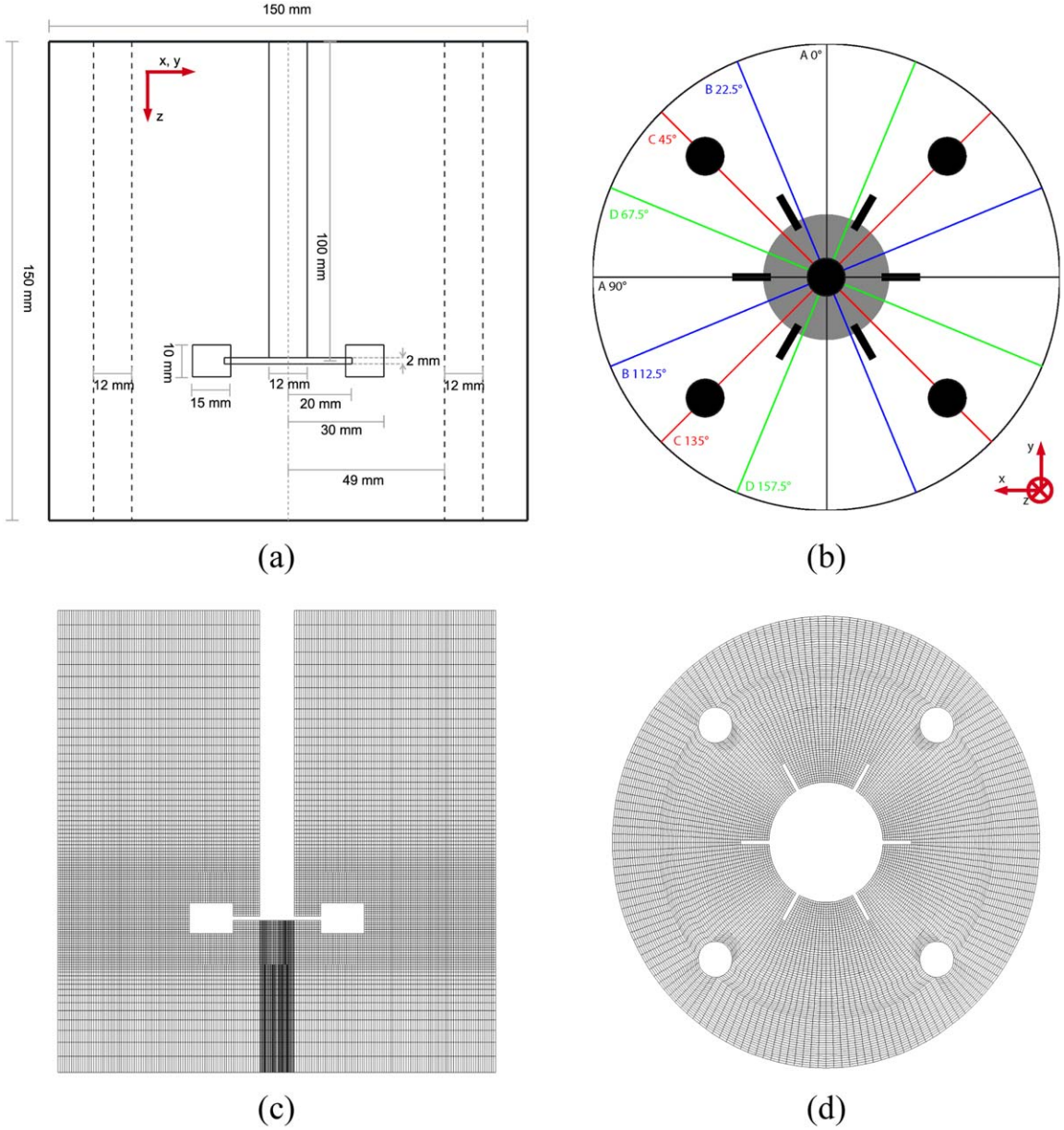

Figure 1. Vertical and horizontal plane view of the stirred tank equipped with four cylindrical baffles and a Rushton turbine (a, b) together with the computational grid used for LES simulations (c, d).

[Color figure can be viewed in the online issue, which is available at wileyonlinelibrary.com.]

aspect ratio of formed aggregates did not change (see Figure 3), which is indicating that populations of formed fragments are rather similar independent whether breakup occurs under turbulent or laminar conditions. Based on the aforementioned observations, we can conclude that this system is ideal to determine the maximum hydrodynamic stresses that are causing aggregate breakup. More information about the breakup experiments can be found in original publications by Soos et al.[8,18]

Large Eddy Simulation of the Stirred Tank

Since no experimental data are available for the used stirred tank geometry LES was used in this study for turbulence characterization. This method is compared to the RANS approach more suitable to predict flow pattern including trailing vortices as well as ε distribution in stirred tanks.[41] Vertical and horizontal plane views of the used stirred tank equipped with four cylindrical baffles and a Rushton turbine is presented in Figure 1a, b. A six-blade Rushton impeller was located at $^1/_3$ of the vessel height measured from the bottom. Unlike the commonly used baffle geometry, with the baffles having rectangular shapes and being attached to the vessel side wall, in this study baffles with rodlike shapes that are not connected to the vessel wall have been used. It is worth noting that such baffle system can be particularly useful for processes when material deposition on the walls is of main concern, e.g., polymer during polymerization reaction. Other applications of such baffle systems include small scale bioreactors applied for cell cultivations where several probes measuring temperature pH, or dissolved oxygen have a similar cylindrical shape.

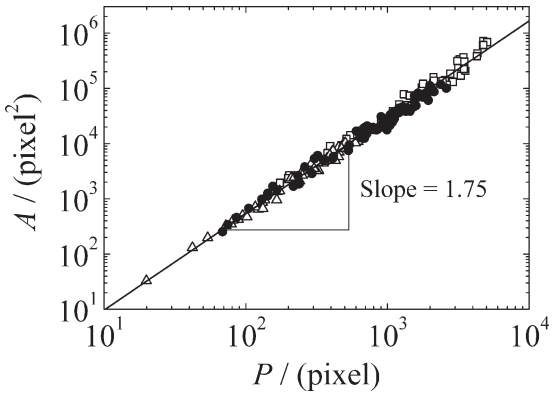

Figure 2. Scaling of area vs. perimeter evaluated from image analysis of formed fragments measured before breakage experiment prepared in stirred tank[18] using stirring speed of 200 rpm and solid volume fraction of 4.10^{-5} (□), at the end of the breakage experiment in stirred tank obtained at stirring speed of 200 rpm and solid volume fraction of 2.10^{-6} (•), and at the end of the breakage experiment in contracting nozzle[8] applying $Re_{nozzle} = 1167$ and solid-volume fraction of 2.10^{-6} (△).

Extracted data were used to evaluate perimeter fractal dimension of the formed clusters which is equal to $d_{pf} = 2/\text{slope} = 1.14$. Consequently the mass fractal dimension was calculated using correlation proposed by Ehrl et al.[66] resulting in d_f equal to 2.7.

The tank was filled with a diluted solution of $Al(NO_3)_3$ at room temperature matching density and viscosity of water, i.e., 1000 kg.m^{-3} and 1.10^{-3} Pa.s, respectively. Simulations were performed for the rotation speed of the impeller N equal to 200 rpm resulting in an impeller Reynolds number of 12,000. The LES simulations were performed using a commercial CFD code FLUENT v6.3. To resolve large velocity gradients near the impeller equal spaced grid with the element size of 0.7 mm was used in the impeller discharge zone while larger element size was used in the vessel periphery (see Figure 1c, d). The computational grid contained approximately 1.6 million elements. The pressure-velocity coupling was solved using PISO scheme while PRESTO! method and bounded central differencing were used for the spatial discretization of pressure and momentum, respectively. A second-order implicit formulation was used to improve accuracy of the transient simulation. The time step used for the simulations was equal to 5.10^{-4} s corresponding to the angular displacement of the impeller zone per time step equal to 0.6°. For convergence criterion a value of 10^{-6} was selected for both continuity and momentum. At each time step the position of the rotating zone relative to the stationary one is recomputed and the grid interface of the rotating zone slides along the interface of the stationary zone. To obtain a statistically converged solution, 10 complete impeller rotations were performed. For each time step eight cross sections (see Figure 1b) were exported from FLUENT and use for later post processing. Taking into account the vessel symmetry, at every time step the vessel field could be split into four quarters, which then were added up to increase the efficiency of the calculation.

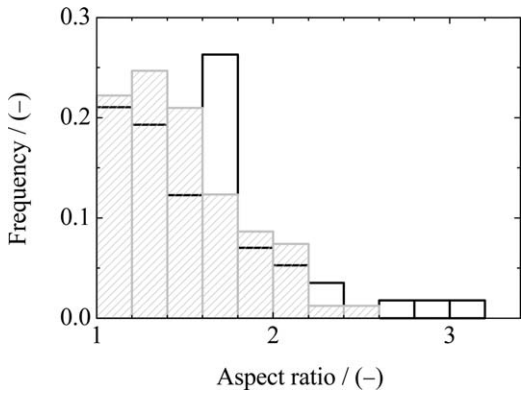

Figure 3. Comparison of the aspect ratio of formed clusters produced during breakage experiment performed in the contracting nozzle (column without pattern), and in the stirred tank (sparse pattern columns).

Turbulence Modeling

The governing equations employed for LES are obtained by filtering the time-dependent Navier-Stokes equations in either Fourier (wave-number) space or configuration (physical) space. The filtering process effectively filters out eddies whose scales are smaller than the filter width or grid spacing used in the computation. The resulting equations thus govern the dynamics of large eddies and they read as follows

$$\frac{\partial \rho}{\partial t} + \frac{\partial}{\partial x_i}(\rho \overline{u}_i) = 0 \tag{1}$$

$$\frac{\partial}{\partial t}(\rho \overline{u}_i) + \frac{\partial}{\partial x_i}(\rho \overline{u}_i \overline{u}_j) = \frac{\partial}{\partial x_i}\left(\mu \frac{\partial \sigma_{ij}}{\partial x_j}\right) - \frac{\partial \overline{p}}{\partial x_i} - \frac{\partial \tau_{ij}}{\partial x_j} \tag{2}$$

where σ_{ij} is the stress tensor due to molecular viscosity defined by

$$\sigma_{ij} \equiv \left[\mu\left(\frac{\partial \overline{u}_i}{\partial x_j} + \frac{\partial \overline{u}_j}{\partial x_i}\right)\right] - \frac{2}{3}\mu \frac{\partial \overline{u}_l}{\partial x_l}\delta_{ij} \tag{3}$$

and τ_{ij} is the subgrid-scale stress defined by

$$\tau_{ij} \equiv \left(\rho \overline{u_i u_j}\right) - \left(\rho \overline{u}_i \overline{u}_j\right) \tag{4}$$

The subgrid-scale stress (Eq. 4) cannot be solved directly and requires modeling.

Subgrid-scale model

The filtering operation in FLUENT is based on the grid spacing. Scales larger than grid spacing are resolved and only the contribution of smaller scales is modeled. The unsolved term in the filtered Navier Stokes equations, i.e., the subgrid-scale stress term (Eq. 4) is modeled following Smagorinsky-Lilly[43,44]

$$\tau_{ij} - \frac{1}{3}\tau_{kk}\delta_{ij} = -2\mu_t \overline{S}_{ij} \tag{5}$$

where μ_t is the subgrid-scale turbulent viscosity. The isotropic part of the subgrid-scale stresses τ_{kk} is added to the filtered static pressure term. $\overline{S}_{ij}$ is the rate-of-strain tensor for the resolved scale defined by

$$\overline{S}_{ij} \equiv \frac{1}{2}\left(\frac{\partial \overline{u}_i}{\partial x_j} + \frac{\partial \overline{u}_j}{\partial x_i}\right) \quad (6)$$

In this study, the turbulent viscosity μ_t is modeled as

$$\mu_t = \rho L_s^2 |\overline{S}| = \rho L_s^2 \sqrt{2\overline{S}_{ij}\overline{S}_{ij}} \quad (7)$$

with L_s being the mixing length for subgrid scales, and $\overline{S}_{ij}$ representing the rate-of-strain tensor for the resolved scale (Eq. 6). FLUENT uses Eq. 8 to determine the mixing length

$$L_s = \min\left(\kappa d, C_s V_i^{1/3}\right) \quad (8)$$

where κ is the von Karman constant, d the distance to the closest wall, C_s the Smagorinsky constant, and V_i the volume of the computed cell.

The original value of the Smagorinsky constant valid for isotropic turbulence is equal to 0.17.[59] In the case of modeling of turbulent flow in the stirred tank values covering range from 0.1 to 0.2 have been applied.[31,42,51,54] Due to the lack of experimental data for studied vessel, the value of the Smagorinsky constant C_s was set to be equal to 0.2 as used previously by Delafosse et al.[54,67] applying the same numerical approach. As it was shown by these authors this value was providing better agreement between their LES simulations and experimental data collected by the same group using stirred tank equipped with Rushton impeller and rectangular baffles connected to the wall.

Data Processing

Postprocessing of the computed velocity fields was performed in MATLAB. The variable computational mesh was mapped onto a regular spaced mesh, *dh* equal to 0.7 mm, to facilitate postprocessing. This resulted in $210 \times 210 = 44{,}100$ grid points per plane. It is worth noting that this mesh size has been chosen according to the smallest size of the FLUENT grid cells which can be found in the impeller discharge zone. All values were interpolated to the new grid with the cubic interpolation method.

Two kinds of fluctuations occur in the impeller region: periodic (or organized) fluctuations, related to the trailing vortices, and random fluctuations corresponding to the resolved part of the turbulent motion. The local instantaneous velocity u_i is, thus, decomposed into its mean, periodic and resolved part of fluctuating terms as follows

$$u_i = \overline{U}_i + \tilde{u}_i + u_i' \quad (9)$$

LES solves for an instantaneous velocity field. In the postprocessing for a given position p of the blades with respect to the baffles, the instantaneous velocity is decomposed into mean, periodic and random part as

$$u_i^{lp} = \overline{U}_i + \tilde{u}_i^p + u'^{lp}_i = \langle u_i^p \rangle + u'^{lp}_i \quad (10)$$

Phase-averaging calculated over number of events was used to calculate at each blade position p the phase-averaged velocity, the turbulent fluctuation and the turbulent velocity correlation. A second statistical treatment over number of blade positions (100 blade positions corresponds to 60°) between the crossing of two blades behind the measurement plane was applied to calculate the mean velocity, the periodic fluctuation for each blade position p and the periodic and turbulent stress tensor.

Similar as in the case of the velocity components discussed earlier, the total kinetic energy was decomposed into two components, i.e., the periodic and the turbulent kinetic energy. Consequently, the total kinetic energy of the flow was calculated as a sum of these two terms as

$$k_{\text{tot}} = k_P + k_T \quad (11)$$

where the periodic kinetic energy k_P, and the turbulent kinetic energy k_T are calculated as follows

$$k_P = \frac{1}{2}\sum_{i=1}^{3}\langle \tilde{u}_i \tilde{u}_i \rangle \quad (12)$$

$$k_T = \frac{1}{2}\sum_{i=1}^{3}\langle u_i' u_i' \rangle \quad (13)$$

The discharge flow of the impeller is characterized by the formation of coherent vortex structures induced by the blade motion. In the case of a Rushton impeller presence of disk results in the formation of two vortices, one above and one below the impeller disk. These vortices have significant impact on mixing because they affect the impeller efficiency. Several methods have been proposed in the literature to identify the center of a trailing vortex. This includes an identification of the point where phase-averaged axial velocity component is equal to zero,[68–72] method based on the vorticity magnitude,[33,42,73] and the method based on the eigenvalues of the tensor $S^2+\Omega^2$, where S and Ω are the symmetric and antisymmetric part of the velocity gradient tensor.[74] While the last one is the most precise as it was shown by Escudie et al.[73] method based on the vorticity magnitude enables to determine the trajectory of the trailing vortices with a good accuracy when compared to the method of Jeong and Hussain.[74] In contrast the method based on phase-averaged axial velocity does not enable to draw correctly the trajectory of the trailing vortex axis. Therefore, the method based on the vorticity magnitude has been used in this study. Briefly, the vorticity, which represents a measure of the rotation of a fluid element, is defined as the curl of the velocity vector

$$\xi = \nabla \times \vec{u} \quad (14)$$

Since FLUENT outputs only the modulus of the vorticity vector, it does not allow to discriminate between the typical two vortices generated above and below the impeller disk, each with opposite sign. Due to this fact the vorticity was evaluated in the postprocessing from the phase-averaged velocity field on the regular spaced grid. Following the procedure presented by Derkse and van den Akker,[42] Sharp and Adrian[33] and Escudie et al.[73], the vorticity normal to the acquisition plane was obtained as follows

$$\omega = \frac{\partial \langle u_r^p \rangle}{\partial z} - \frac{\partial \langle u_z^p \rangle}{\partial r} \quad (15)$$

where u_r and u_z represent the radial and axial velocity component, respectively. The vorticity is normalized with the velocity at the blade tip U_{tip} through

$$\xi = \frac{\omega T}{U_{tip}} \equiv \frac{\omega T}{\pi N D} \quad (16)$$

where N the impeller rotation speed, T the tank diameter, and D the impeller diameter. As mentioned previously and as shown previously[33,42,67,73] this definition enables to discriminate the two vortices generated above and below the

disk. Since the values of the vorticity of the upper and lower vortex are positive and negative, respectively, the center of the upper vortex corresponds to the maximum value while center of the lower vortex to the minimum value of the vorticity.

The turbulent energy dissipation rate ε, was the last turbulent quantity evaluated from the LES data. A direct estimation of ε could be performed from measurements of turbulent velocity gradients in the three directions according to

$$\varepsilon = \nu S_{ij} S_{ij} = \frac{\nu}{2}\left(\frac{\partial u_i}{\partial x_j} + \frac{\partial u_j}{\partial x_i}\right)^2 \tag{17}$$

However, as LES is not resolving the smallest scales of the velocity field the direct determination of the dissipation rate via LES is not possible. Therefore, assuming a local equilibrium between production and dissipation of turbulent kinetic energy at the cut-off scale, the subgrid dissipation rate was computed according to

$$\varepsilon_{SGS} = \tau_{ij} S_{ij} = 2\mu_t S_{ij} S_{ij} = \frac{\mu_t}{2}\left(\frac{\partial u_i}{\partial x_j} + \frac{\partial u_j}{\partial x_i}\right)^2 \tag{18}$$

and the total dissipation rate (of the solved and the subgrid scale) was evaluated as follows

$$\varepsilon_{SGS} = 2(\mu_t + \mu) S_{ij} S_{ij} = \frac{\mu_t + \mu}{2}\left(\frac{\partial u_i}{\partial x_j} + \frac{\partial u_j}{\partial x_i}\right)^2 \tag{19}$$

In similar way as for the velocity and the kinetic energy, phase-averaging and ensemble-averaging was performed also for turbulent energy dissipation rate.

The tank energy dissipated in the whole system was calculated from the ratio of the power input P_{impeller}, calculated as the torque on the impeller and shaft multiplied by the angular velocity,[75] and mass of the liquid m, according to

$$\langle \varepsilon \rangle = \frac{P_{\text{impeller}}}{m} = \frac{\Omega \int_{\mathbf{A}} \mathbf{r} \times (\tau \cdot \mathrm{d}\mathbf{A})}{m} \tag{20}$$

Here $\mathbf{A}$ stands for the surface of impeller and shaft, Ω is the angular velocity vector (in rps), $\mathbf{r}$ is the position vector, τ is the stress tensor, and $\mathrm{d}\mathbf{A}$ is the differential surface vector. In parallel, $\langle \varepsilon \rangle$ was evaluated also from the local values calculated for individual planes A-D by weighting the individual contribution of each plane.

Results and Discussion

As an example of the flow a snapshot in the horizontal plane slicing through the impeller position is presented in Figure 4a. It can be seen that close to the impeller the flow is highly correlated to the impeller blade positions. There is a clear formation of trailing vortices behind the blades. When evaluating the velocity magnitudes inside the trailing vortices it was found that these are substantially higher than the impeller tip speed reaching maximum values around $1.9 \times U_{tip}$. Due to the presence of baffles the movement of the fluid in radial direction generated by the impeller is much stronger for blade positions in-between baffles as compared to the situation where the blades are in-plane with the baffles. This effect can be also seen in the vertical planes located midway between two baffles Figure 4b1–b3 and passing through baffles Figure 4c1–c3. In the first case the turbulent vortex structure extend almost to the vessel wall. When baffles are present however, the vortices strongly interact with them leading to substantial reduction of the radial flow (also seen in Figure 4a). Behind the baffles the flow is mostly tangential, however, small eddies resulting from the breakup of large vortices on the baffles are still present.

Mean velocity

The local velocity profiles were used in the next step to calculate the phase-averaged quantities. In Figure 5 a comparison of mean radial, tangential and axial velocity components are presented evaluated for planes A, B, C, and D (see Figure 1). Since there are no available experimental data which could be used to validate our LES results and to discuss the effect of cylindrical baffles on the phase-averaged velocity components, we include here experimental data of Wu and Patterson[29] measured in the stirred-tank equipped with rectangular baffles connected to the vessel wall using the laser-Doppler anemometry (see Figure 5a1–a3). As can be seen from Figure 5a1 the highest values of the radial velocity can be found close to the impeller tip with decreasing values for increasing the radial distance from the impeller. However, the magnitude of the radial velocity component is at all radial positions lower than that measured by Wu and Patterson.[29] Furthermore, when comparing the radial velocity magnitude for radial positions ahead of the baffles, e.g., $r/R = 1.08-1.5$ the difference is approximately 25% while it increases up to approximately 50% at $r/R = 2.26$, corresponding to the region behind the baffle. Even though a certain reduction of the maxima of could be related to the increase of the impeller blade thickness[76] we believe that the observed reduction of U_r/U_{tip} maxima is in our case caused by the shorter distance between impeller and baffles compared to the setup investigated by Wu and Patterson.[29] When considering the radial outflow stream generated by the impeller it was found that this is moving slightly upward, which is a well-known observation for impellers with low clearance from the vessel bottom.[29,77] While the spreading rate in close vicinity of the impeller is comparable to that measured by Wu and Patterson,[29] it increases substantially at larger radial distance. Presumably this is an effect of the baffles which are located closer to the impeller so they affect the flow earlier compared to standard setup.

In the case of tangential velocity (see Figure 5a2) one can see that the maxima of U_t/U_{tip} are comparable to those measured by Wu and Patterson[29] while substantial differences can be observed for values at the discharge stream periphery. While in the case of Wu and Patterson[29] they reached values around zero in our case values of U_t/U_{tip} between 0.1 to 0.2 can be found. This indicates that cylindrical baffles, even though located closer to the impeller, are not as efficient as baffles connected to the vessel wall in preventing the flow from picking up tangential movement.

A comparison of axial velocity profiles evaluated at various radial positions with data measured by Wu and Patterson[29] is presented in Figure 5a3. It can be seen that in the region ahead of baffles the obtained values of U_{ax}/U_{tip} following trend similar to that measured by Wu and Patterson[29] with fluid flowing from top downward in the zone above the impeller and flowing from bottom upward in the zone below the impeller. Due to the location of the baffles closer to the impeller as compared to the setup used by Wu and Patterson[29] the point where is close to zero is reached much earlier

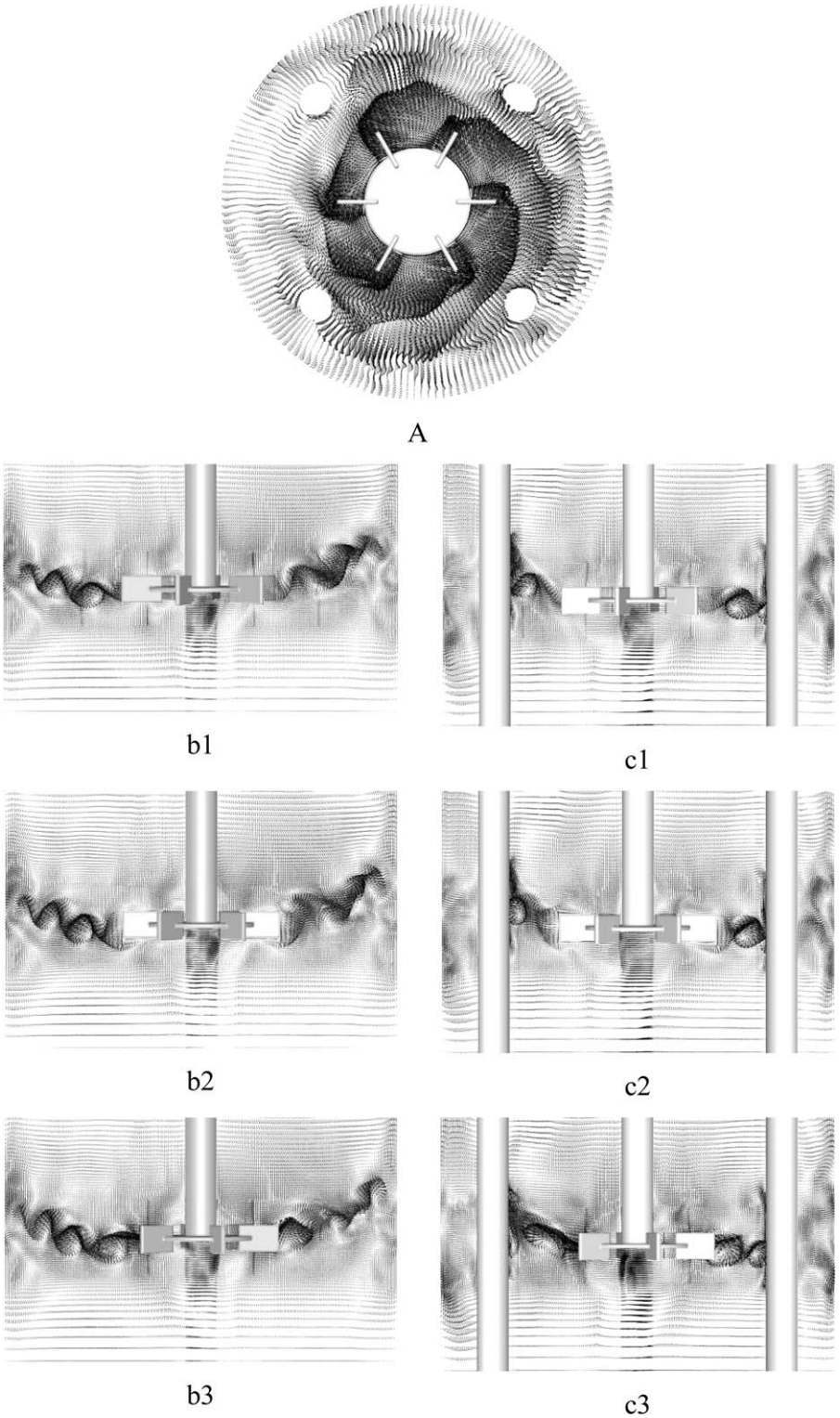

Figure 4. Example of an instantaneous velocity vector plots (a) top view, (b and c) side view corresponding to relative angle −15°, 0° and +15°, respectively.

Left column corresponds to the view plane located midway between two baffles while right column corresponds to the view plane passing through baffles.

(see Figure S1 online in additional Supplementary Material). At radial position $r/R = 2.26$, which is the region located behind the cylindrical baffles, the discharge stream is split into two parts one flowing upward while the other is flowing downward with respect to the impeller disk plane. Even though this pattern with two circulation loops one above and one below the vertical impeller plane is comparable to that generated by the radial impeller we found that absolute values of U_{ax}/U_{tip} are substantially higher compared to those measured by Wu and Patterson.[29] When comparing the

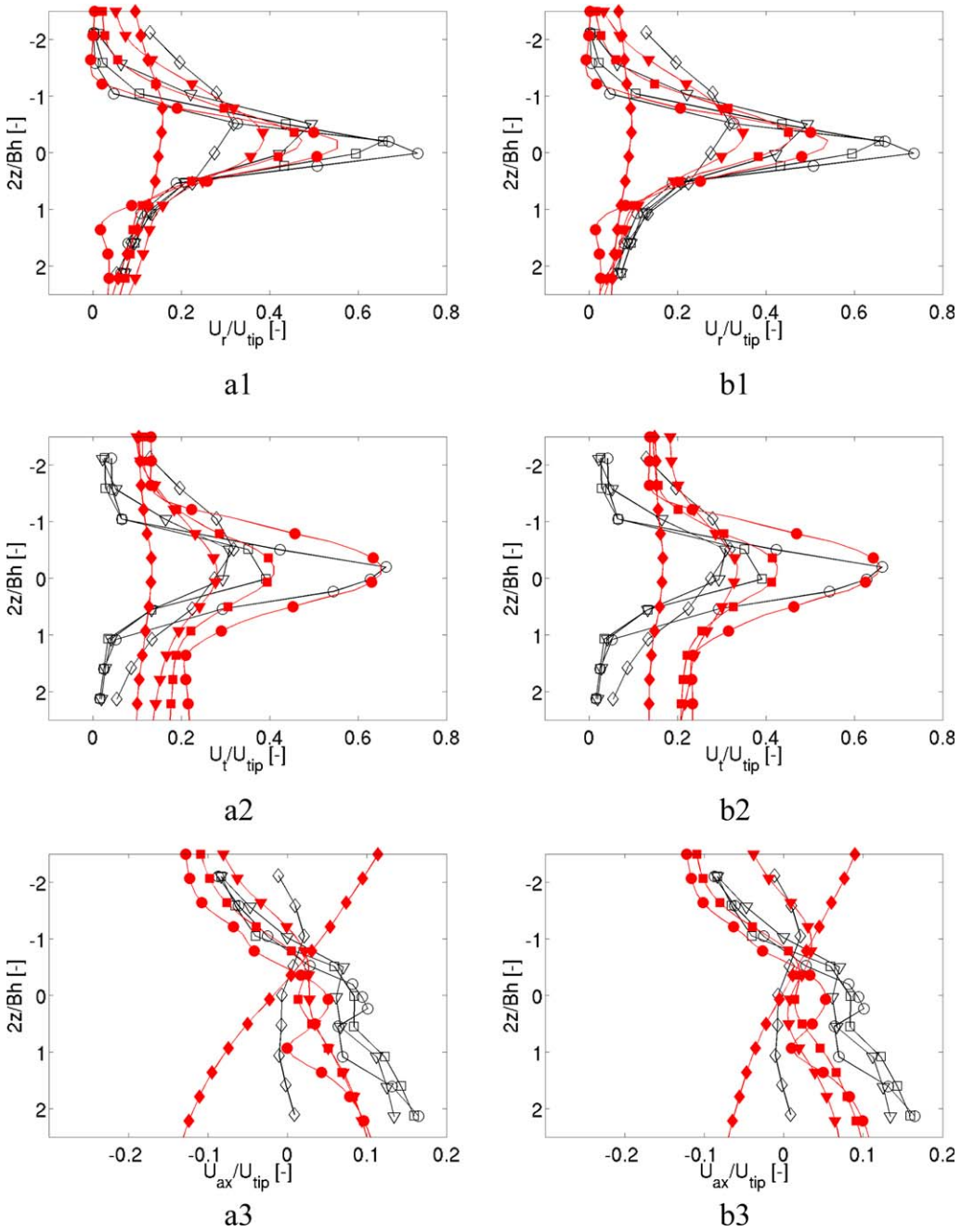

Figure 5. Comparison of mean radial (top row), tangential (middle row), and axial (bottom row) velocity components evaluated from LES (closed symbols) at radial position of r/R=1.08 (•○), r/R=1.29 (■,□), r/R=1.50 (▲,△), r/R=2.26 (◆,◇) for plane A (left column) and plane C (right column).

All velocity components were normalized by U_{tip}. For comparison experimental data of Wu and Patterson[29] (open symbols) are presented as well. [Color figure can be viewed in the online issue, which is available at wileyonlinelibrary.com.]

velocity components for plane C (Figure 5b1–b3) with those measured for plane A (Figure 5a1–a3) it can be seen that at $r/R = 1.08$ and 1.29 they are comparable to those calculated for plane A while larger differences can be observed for larger distances from the impeller tip for $r/R = 1.50$ and 2.26. It is noteworthy that velocity profiles for the two planes B and D are quite similar to those measured for plane A (data not shown).

All these results indicate that cylindrical baffles located closer to the Rushton impeller affects substantially the flow pattern generated in the stirred tank. Due to the shorter distance between the impeller blades and the baffles the radial velocity component is reduced while the broadness of the discharge stream is increased. Since there is free space behind the baffles where fluid can pass the tangential velocity components are systematically higher compared to the system where tangential fluid motion is stopped by baffles connected to the vessel wall. Furthermore, substantially different axial velocity profile was observed below the impeller and behind the baffles.

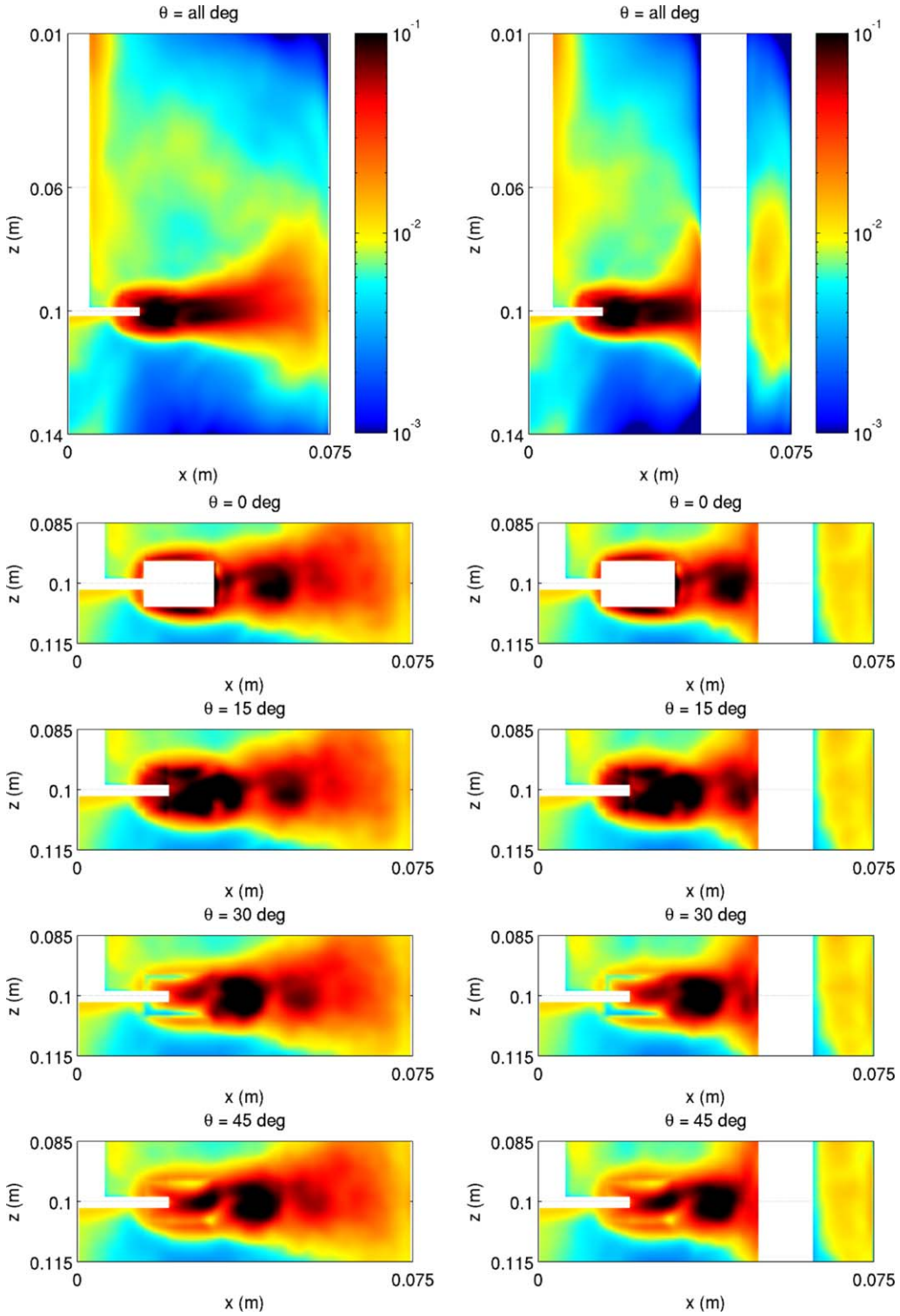

Figure 6. Comparison of normalized average total kinetic energy $\langle k_{tot}^{\theta} \rangle / U_{tip}^2$ for plane A (left column) and plane C (right column).

[Color figure can be viewed in the online issue, which is available at wileyonlinelibrary.com.]

Kinetic energy

Velocity fluctuations in a turbulent flow generated by the impeller are composed of a periodic part and a random part, also called the turbulent part. It must be kept in mind that LES only partially resolves the random part. Consequently, the kinetic energy contained in the velocity fluctuations can be also divided into a random and periodic part. Phase-resolved contour plots of total kinetic energy, obtained by summation of periodic and resolved turbulent kinetic energy, evaluated at planes A and C are presented in Figure 6. It can be seen that in the case of plane A, located midway between two baffles, the region of elevated k_{tot}^{θ} extends over a longer

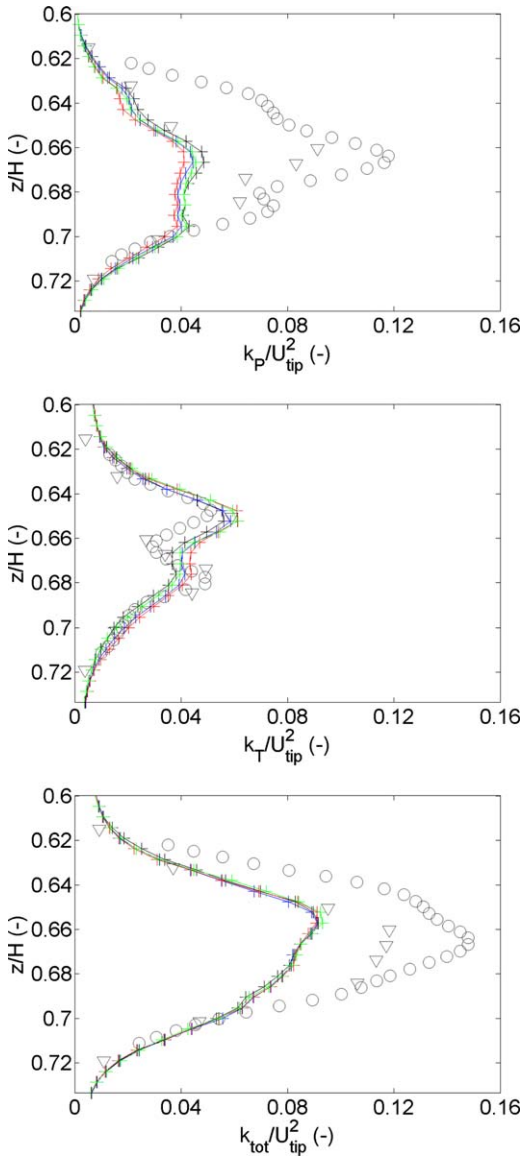

Figure 7. Comparison of periodic (top row), turbulent (middle row), and total (bottom row) kinetic energy normalized by U_{tip}^2 evaluated at radial position of r/R=1.08.

Lines represent data calculated with LES while points corresponds to the experimental data of Escudié and Liné[34] (○) and Wu and Patterson[29] (▽). [Color figure can be viewed in the online issue, which is available at wileyonlinelibrary.com.]

distance from the impeller as compared to plane C where this zone is shortened due to presence of the baffle. This effect is similar to that observed from velocity snapshots (see Figure 4). A summary of phase-averaged profiles of kinetic energy evaluated at radial distance $r/R = 1.08$ from the impeller for all planes A-D is presented in Figure 7. For comparison, data measured by Escudié and Liné[34] and Wu and Patterson[29] are included as well. It can be seen that similarly to the velocity profile there is difference in k_p^θ between the experimental and our LES data, while very good agreement was found for the random part of the kinetic energy k_t^θ. Since k_{tot}^θ is obtained as summation of k_p^θ and k_t^θ, there is also a difference between the LES data and the experimental data. According to the results of Rutherford et al.,[76] the differences in k_p^θ can be related to the larger blade thickness, t_b of the used $(t_b = 0.025D)$ impeller which is two times larger than that used by Escudié and Liné.[34] On the other hand, no effect of the increased impeller thickness on the turbulence was observed, resulting in comparable values of k_t^θ to those measured for the Rushton impeller with thinner impeller blades mounted in fully baffled vessels.

Energy dissipation rate

As it was discussed in the introduction the energy dissipation rate is quantity controlling many processes including mixing, chemical reactions, aggregation, breakup, etc. Even though the volume-averaged value of $\langle\varepsilon\rangle$ is a very useful quantity, commonly applied for scaling of stirred vessels, as discussed in the introduction, the distribution of the local is very heterogeneous within stirred tanks. This is clearly demonstrated in Figure 8 where the phase-averaged ε normalized by N^3D^2 is plotted for plane A and C. It can be seen that the highest values of ε are typically located in the vicinity of impeller while substantially lower values can be found at the reactor periphery covering a range of more than four-orders of magnitude. It is worth noting that ε distribution in planes B and D are comparable to that obtained for plane A.

To support validity of the presented results obtained values of ε together with k_{tot} described previously were used to evaluate Taylor microscale λ, in the studied stirred tank (see Figure S2 online). Since this length-scale is commonly used as a boundary below which the flow is strongly affected by the viscosity, to adequately resolve turbulence in the simulations it is important to keep the mesh size comparable to λ. It was found that in the stream generated by the impeller values of λ are in the range of 0.55–1.5 mm, while outside of the jet values as large as 5 mm have been observed. These values are comparable with the size of the computational grid equal to 0.7 mm used in this work which supports the validity of the presented results.

To quantify the overall amount of the energy introduced in the system the vessel-averaged energy dissipation rate can be estimated from the information obtained for individual planes A-D. It was found that surface averaged values of ε from planes A, B, and D are very comparable while for plane C higher values of approximately by 50% were obtained. Taking this variation into account, the vessel-averaged ε was calculated as a volume contribution of the region around the baffles, assuming circular sector being tangential to the baffles and characterized by ε values as evaluated for plane C. For the rest of the vessel ε values calculated for plane A, has been used. In this way $\langle\varepsilon\rangle$ was equal to 0.034 m^2/s^3. This value is very close to that determined from the torque acting on the impeller and shaft surface (Eq. 20) resulting in $\langle\varepsilon\rangle$ equal to 0.037m^2/s^3 further indicating that used mesh size was adequate. To compare the power consumption in the studied geometry with literature data obtained for baffles connected to the vessel wall, the corresponding Power number Po was evaluated. It was found to be equal to 3.34 which are substantially lower than those reported for fully baffled system with Po ranging from 4.6 to 5.9.[78,79] This can be explained by the weaker overall effect of the used cylindrical baffles. They do not stop the tangential fluid motion completely leading to lower energy

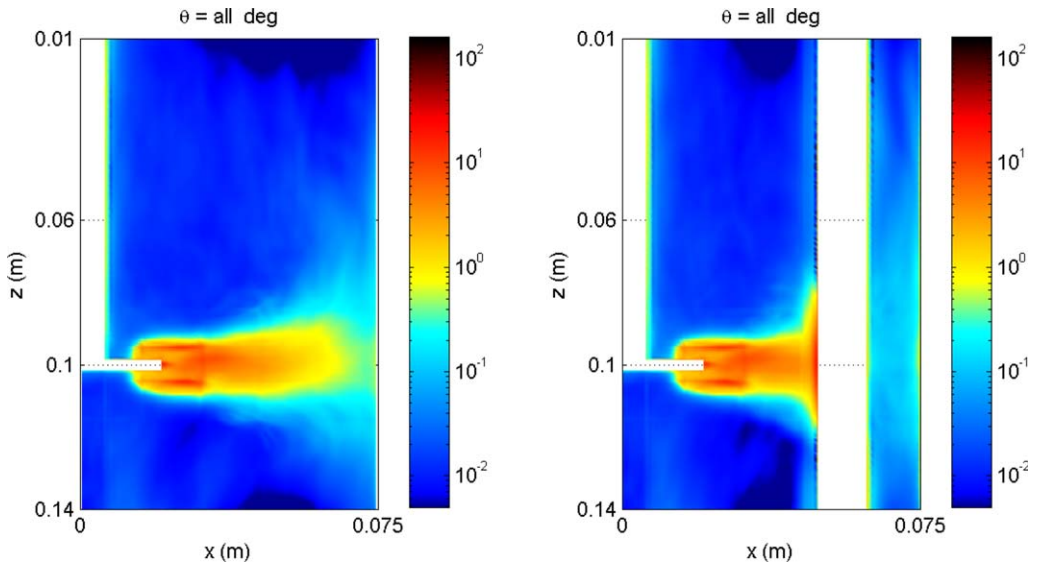

Figure 8. Angle-averaged normalized energy dissipation rate $\bar{\varepsilon}/N^3D^2$ plotted for plane A (left) and C (right).

[Color figure can be viewed in the online issue, which is available at wileyonlinelibrary.com.]

dissipation. In addition, further reason for lower *Po* could be application of thicker impeller blades with respect to the impeller diameter.[76]

To access the variation of local ε as a function of impeller blade position, contour plots of the phase-resolved energy dissipation rate ε^θ, normalized by N^3D^2 evaluated at various relative positions of the impeller to the acquisition plane is presented in Figure 9 for plane A, and in Figure 10 for plane C, respectively. It can be seen that highest values of ε^θ exceeding $100{\cdot}N^3D^2$ can be found around the impeller blade edge and in the wake behind the impeller blade followed by a decrease of the ε^θ magnitude for larger angles. Moreover, when the impeller blades are close to the baffles, additional hot spots with very high ε^θ can be found at the point where the discharge zone impacts the baffle, with magnitudes comparable to those found near the impeller (see Figure 10). The variation of the normalized maxima of ε^θ as a function of the angular position is summarized in Figure 11 for all four acquisition planes A, B, C, and D. The profiles have approximately the same average values of $\varepsilon^\theta_{\max}/N^3D^2$ close to 35, however, with substantial variation with angular position. The maximum of ε^θ approximately equal to $130\pm13\cdot N^3D^2$ was found for angles between 2 to 6° behind the impeller blade while minima with values ranging from $10\cdot N^3D^2$ (for planes A, B and D) to $25\cdot N^3D^2$ (for plane C) were observed in the region approximately 50° behind the impeller blades (see Figure 11). It is worth noting that this difference is due to presence of baffle in the plane C located closer to the impeller with a hot spot of higher ε^θ at point of fluid impact. To further indicate the variation of the ε^θ in Figure S3 are presented radial profiles of the normalized energy dissipation rate at the impeller midsection passing through the impeller disc evaluated for plane A and C. It was found that for angles when impeller blade is passing the investigated plane highest values of the normalized energy dissipation rate are located at the impeller blade edge. With the moving of the impeller blade in angular direction the investigated plane maximum values ranging from 4 to 15 have been observed in the impeller discharge zone (see online for Figure S3). While the magnitude of these values is in agreement with those reported by other authors obtained either from experiments or numerical simulations,[31,32,34,54,80] due to the smaller impeller diameter with respect to the tank diameter the radial positions of maximum values are shifted toward higher radial r/T compared to those reported by other authors.

When comparing the absolute values of $\varepsilon_{\max}/N^3D^2$ presented in Figures 9 and 10 with other data in the literature it was found that calculated values from this study are very close to those published by Yianneskis group[31,51] as well as measurement of the maximum shear rate $\gamma_{\max}$, of Wichterle et al.[40] resulting in $\varepsilon_{\max}/N^3D^2$ equal to 80 and 100, respectively. On the other hand, lower values of $\varepsilon_{\max}/N^3D^2$ about 30 were reported by Derksen and van den Akker.[42] This difference can be attributed to the coarser grid used by Derksen and van den Akker[42] whose mesh spacing at the impeller blade was about 75 wall units compare to about 15 wall units applied in this study. When comparing size of the computational grid used in this work with that applied by Yeoh et al.[51] and Micheletti et al.[31] we found that our spatial resolution in the impeller discharge zone was about 15 times the mean Kolmogorov scale while slightly large mesh size in the order of 30 times the mean Kolmogorov scale was applied by Yeoh et al.[51] and Micheletti et al.[31] This also justifies slightly higher values calculated from our LES.

Trailing vortices

Trailing vortices represent a flow structure which is developed in the wake of a Rushton impeller blade, and is then advected by the impeller stream into the bulk of the tank. As it was shown by several authors[33,42,67,71,73] the core of a trailing vortex is characterized by the high level of turbulent kinetic energy. This is due to the transfer of the energy between periodic motion and turbulence which occurs in the trailing vortex core. To identify whether same can be concluded also for the nonstandard tank geometry used in this work, position of the center of the trailing vortices was determined using vorticity magnitude approach described previously.

Phase-resolved contour plots of the vorticity magnitude evaluated for four different angles at two planes A and C are presented in Figure 12. A pair of counter rotating vortices is

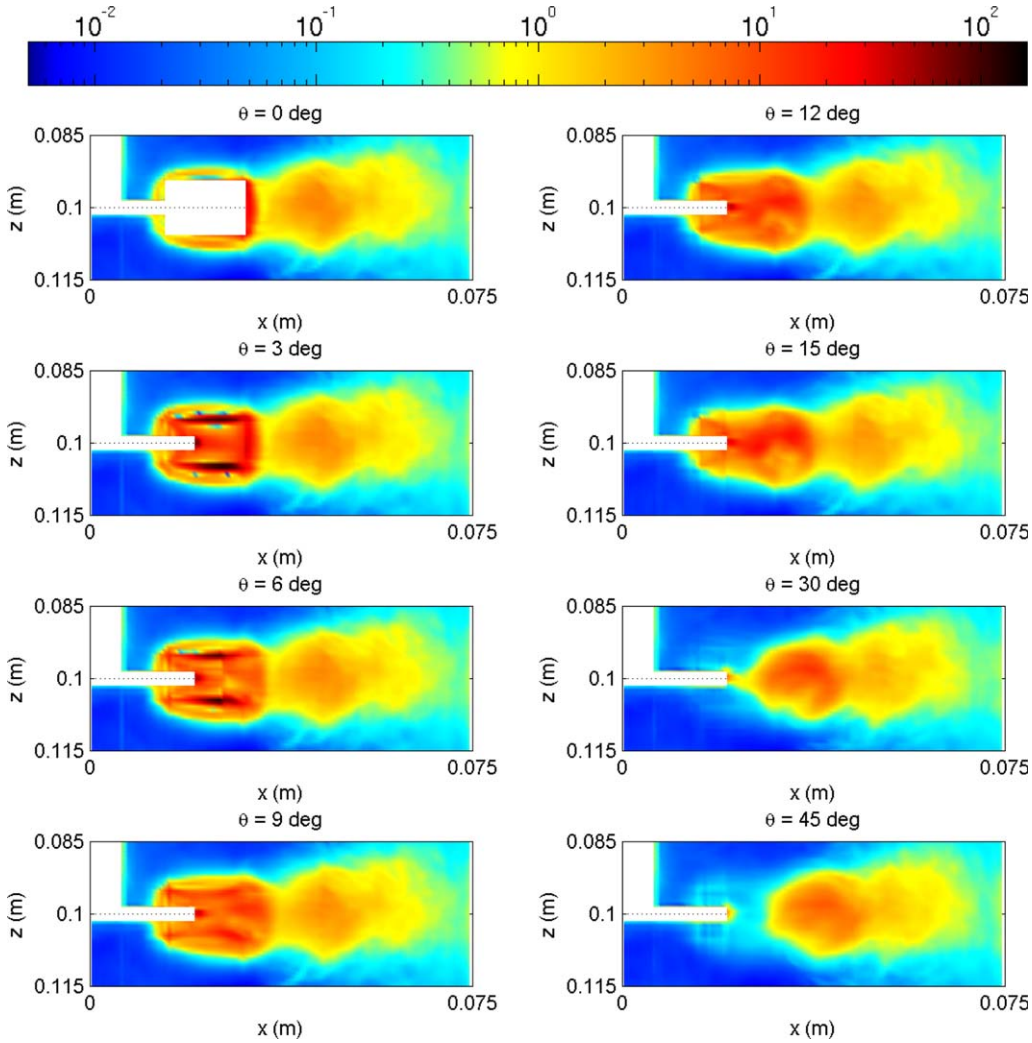

Figure 9. Angle-resolved, event-averaged normalized energy dissipation rate $\langle \varepsilon^{\theta} \rangle / N^3 D^2$ plotted at various angles with respect to impeller blade.

Presented results correspond to plane A. [Color figure can be viewed in the online issue, which is available at wileyonlinelibrary.com.]

clearly visible where the upper vortex rotates counterclockwise while the lower vortex rotates in a clockwise direction. For plane A, which is located between two baffles, they move radially without visible deformation. In plane C, when vortices reach the baffle surface their radial movement is stopped leading to their rapid elongation and increase of their respective center separation (see Figure 12). It is interesting to point out that despite their large deformation they are persistent over a rather large angular distance. Furthermore, when comparing the position of the trailing vortices in the impeller discharge zone from Figure 12 with ε contour plots presented in Figure 9 and 10 it was found that position of the maxima of ε^{θ} closely correlates with the position of trailing vortices. It is worth noting that the same results were observed also by other authors when analyzing the flow generated by the Rushton impeller.

To compare the action of baffles studied in this work to the baffles connected to the vessel wall in Figure 13 a comparison of the location of the trailing vortex axis evaluated from our LES together with experimental data of Derksen and van den Akker[42] and Escudié and Liné[73] is presented. It can be seen that in our case the radial expansion of vortices is suppressed as compared to the experimental data with baffles connected to the wall. The phenomenon observed previously, when high-vorticity magnitude was found at the baffle wall is reflected also in the projection of the core of trailing vortices. For plane C, i.e., passing through the baffles, there is sudden jump in the location of the vortex center located on the baffle surface (see also Figure 12).

Scaling of maximum stable aggregate size with ε_{max}

According to a fracture-mechanics model developed by Zaccone et al.[26] breakup of fractal aggregates occurs when energy supplied through the hydrodynamic stress exceeds the energy required to extend the surface energy of an initial crack into an aggregate resulting in its breakup. Even though such a model is capable to predict scaling of aggregate size as a function of the applied stress, it is not capable to provide information about the absolute value of the stress responsible for aggregate breakup. It is, therefore, the goal of this work to complete this picture and combine the founding of Zaccone et al.[26] with maximum stress analysis present in a stirred tank.

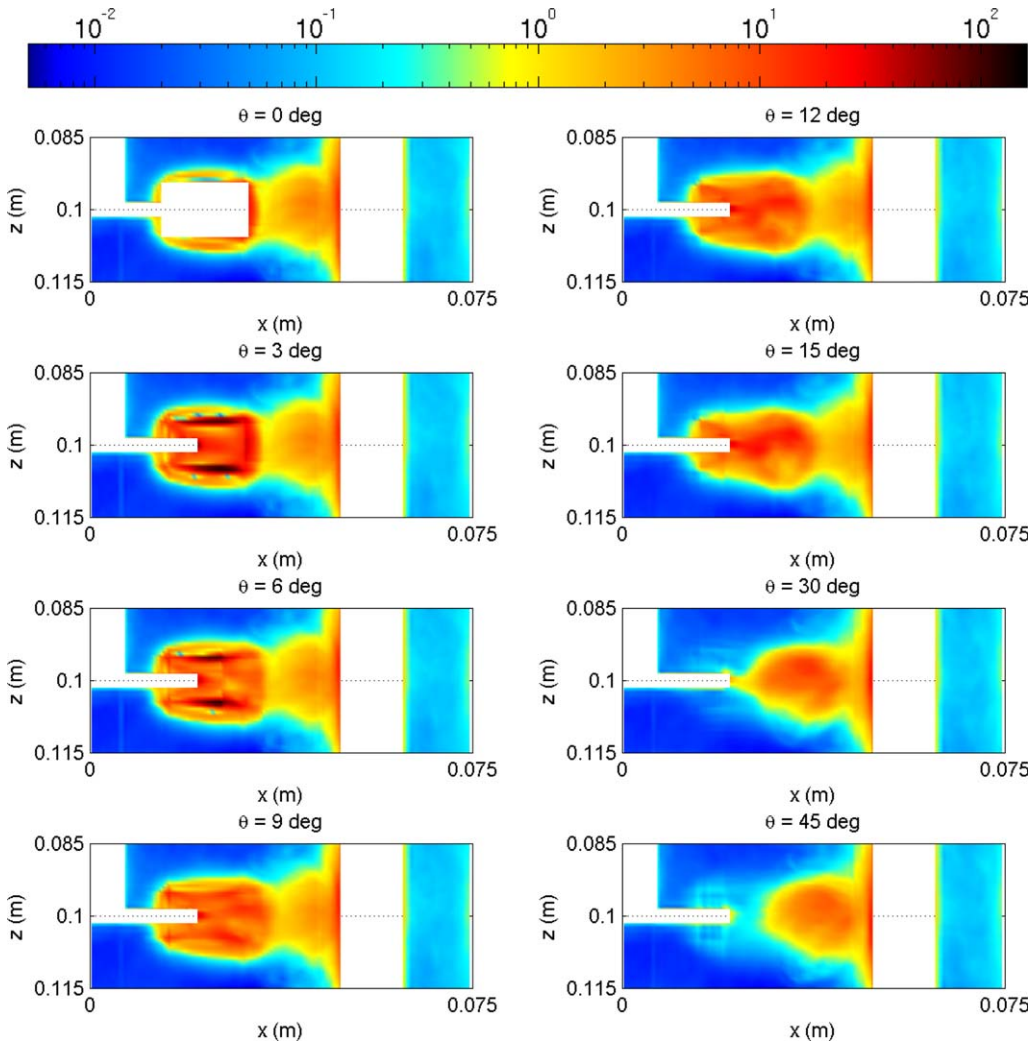

Figure 10. Angle-resolved, event-averaged normalized energy dissipation rate $\langle \varepsilon^{\theta} \rangle / N^3 D^2$ plotted at various angles with respect to impeller blade.

Presented results correspond to plane C. [Color figure can be viewed in the online issue, which is available at wileyonlinelibrary.com.]

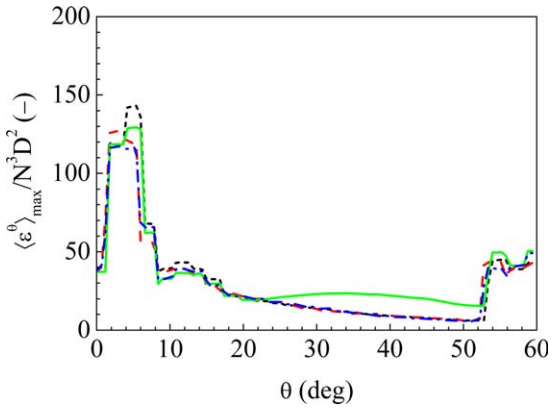

Figure 11. Comparison of the angular variation of the normalized maximal dissipation rate $\langle \varepsilon^{\theta} \rangle_{max} / N^3 D^2$ evaluated for four different planes: plane A (short-dash line), plane B (dash line), plane C (solid line), plane D (dash-dot line).

[Color figure can be viewed in the online issue, which is available at wileyonlinelibrary.com.]

To relate the observed values of ε_{max} to our previous breakage data measured in a stirred tank by Soos et al.[18] in Figure 14 we present the scaling of the maximum stable mean radius of gyration of formed fragments plotted as a function of the maximum hydrodynamic stress $\tau_{max} \left(= \sqrt{\mu \rho \varepsilon_{max}} \right)$ evaluated from ε_{max}, which is shown in Figure 11. In the same figure the maximum stable aggregate sizes measured after breakage experiments in a contracting nozzle are also presented.[8] They are plotted as a function of the maximum hydrodynamic stress that occurs in the nozzle[8] (see Figure 14). It is worth noting that since the same initial aggregates were used in both breakage experiment and no restructuring was present resulting in the same d_f equal to 2.7 according to the fracture model of Zaccone et al.[26] both data sets should follow the same scaling. As can be seen both data sets do not follow only the same scaling but also fall on top of each other indicating that the maximum hydrodynamic stress responsible for the breakup is independent whether the flow was laminar or turbulent. Furthermore, the size of Kolmogorov microscale evaluated using ε_{max} from

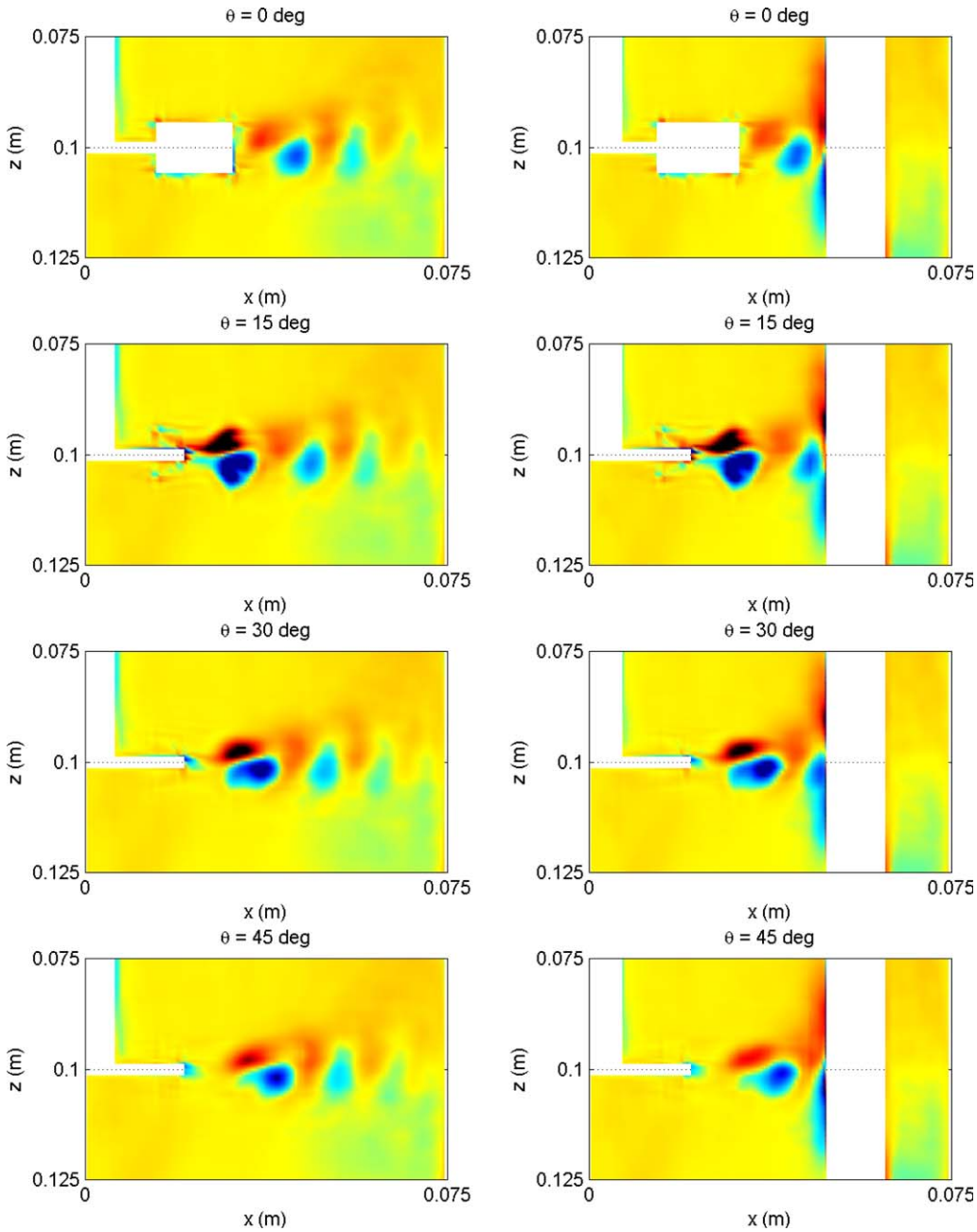

Figure 12. Comparison of phase-averaged vorticity magnitude $\langle \xi^{\theta} \rangle$ for plane A and C.

[Color figure can be viewed in the online issue, which is available at wileyonlinelibrary.com.]

our LES data, and the size of formed fragments are very comparable indicating that breakup of aggregates even under such high values of ε_{max} occurs within Kolmogorov eddies.

The used aggregates are very fragile and break instantaneously, i.e., on the shortest time scale of the flow, when they are exposed to the high values of the hydrodynamic stress. A simple test to probe for the aforementioned high values of ε could be to measure the time needed for the system to reach maximum steady state size during a breakage experiment. To estimate this time from our LES data we evaluate the flow rate of the liquid passing through the area with ε_{max}, corresponding to $130 \cdot N^3 D^2$. Since the axial components of the velocity are substantially smaller compared to the radial and tangential parts, they were omitted from the calculation. Furthermore, only fluctuating part of the local velocity, calculated by subtracting mean velocity from the instantaneous one at every time point, was considered in the calculation. In this case statistical averaging over a number of realizations was performed. Such velocity component, i.e., radial or tangential, was multiplied by a projected area of ε_{max} in radial and tangential direction resulting in a flow rate of the fluid passing through the zone of ε_{max}. Since it is assumed that aggregates break instantaneously when exposed to high values of the hydrodynamic stress, the corresponding time needed to reduce the size of all aggregates present in the stirred tank would be equal to the time needed to pump the whole vessel content through the zones with ε_{max}. It was found that this time is equal to approximately 60 min for conditions used in this study, i.e., stirring speed of 200 rpm. This time is in good agreement with time measured by

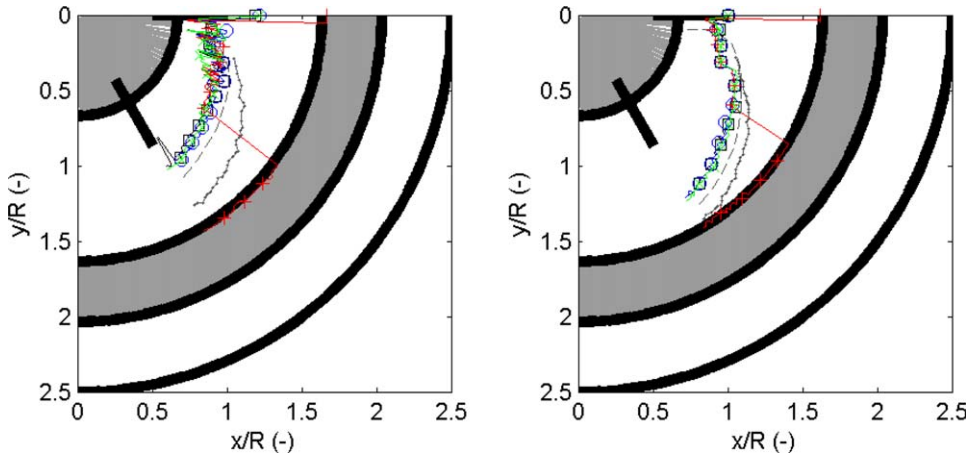

Figure 13. Comparison of the location of axis of the upper (left) and the lower (right) trailing vortex.

Plane A (□), plane B (○), plane C (+), plane D (×). Experimental data of Escudié and Liné[73] (—) and Derksen and Van den Akker[42] (− −) measured for rectangular baffles attached to the vessel wall are plotted for comparison. [Color figure can be viewed in the online issue, which is available at wileyonlinelibrary.com.]

Kusters et al.,[81,82] who report approximately 40 min required to break all aggregates in a stirred tank. This is a further confirmation that the extreme and not the average values of ε are relevant when considering processing suspension of containing dispersed particles. Similar conclusions were reported by other authors[83,84] when studying droplet breakup and found that the maximum stable droplet size scales with the maximum energy dissipation rate present in the system.

Conclusions

In this study large eddy simulations (LES) were used to model the flow field in a stirred tank equipped with the Rushton turbine (RT) and four cylindrical baffles not connected to the wall. It was found that the used baffles have a significant effect on the radial velocity profile and on the expansion of the trailing vortex structure, while the flow field in the impeller vicinity is very comparable to that of standard setups with RT and rectangular baffles connected to the wall. Due to the larger blade thickness combined with the more central location of the baffles, the periodic part of the kinetic energy was found to be substantially lower than that measured in stirred tanks equipped with a standard RT impeller. On the contrary, no significant effect on the turbulent kinetic energy was found. Phase-resolved energy dissipation rates ε indicate its large variation with highest values located at the impeller blade edges and in the wake behind the impeller, with maximum values reaching magnitudes of $130 \pm 13 \cdot N^3 D^2$. When aggregate size is plotted against peak values of the corresponding maximum hydrodynamic stress $\tau_{max}\left(=\sqrt{\mu\rho\varepsilon_{max}}\right)$, located approximately 2 to 6° behind the impeller blades, the maximum stable aggregate sizes measured in the stirred tank closely correlate with comparable breakage data obtained under laminar conditions. This indicates that the same mechanism was involved in the aggregate breakup independent whether the flow was laminar or turbulent. Furthermore, obtained results indicate that once the proper scaling of the maximum stable aggregate sizes versus the maximum hydrodynamic stress is known this allows us to predict the breakup behavior of the same aggregates in the other vessel geometries— independent whether it is operating under laminar or turbulent conditions.

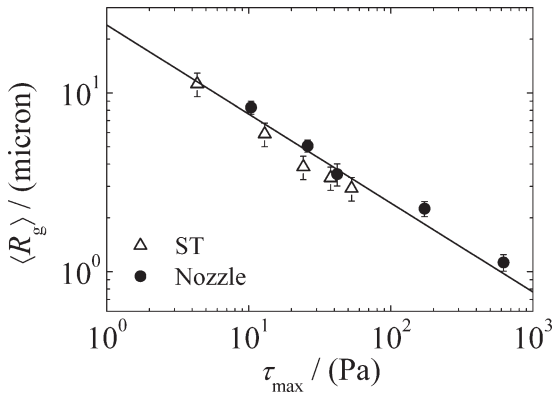

Figure 14. Scaling of the maximum stable aggregate size measured at the end of breakage experiment using contracting nozzle and stirred tank plotted as a function of the maximum hydrodynamic stress present in the system.

Values of τ_{max} for contracting nozzle were taken from Soos et al.[8] while those used to plot stirred-tank data were evaluated from LES presented in this work. Line represents the theoretical scaling calculated from a fracture-mechanics model developed by Zaccone et al.[26] using a fractal dimension d_f equal to 2.7 extracted from image analysis of formed clusters (see Figure 2).

Acknowledgment

Authors thank to Prof. Dr. Massimo Morbidelli and Thomas Villiger for valuable comments and suggestions. This work was financially supported by Swiss National Science Foundation (Grant 200020_147137/1).

Notation

A = surface of impeller and shaft, m^2
A = projected surface area, $pixel^2$
C_s = Smagorinsky constant

d = distance to the closest wall, m
d_f = mass fractal dimension
d_{pf} = perimeter fractal dimension
dh = interpolation mesh size, m
D = impeller diameter, m
k_p = periodic kinetic energy, m^2/s^2
k_T = turbulent kinetic energy, m^2/s^2
k_{tot} = total kinetic energy, m^2/s^2
$\langle k_i^p \rangle$ = phase-average kinetic energy for any blade position, m^2/s^2
k_i^θ = phase-resolved kinetic energy
Ls = mixing length for subgrid scales, m
N = impeller rotation speed, s^{-1}
P = aggregate perimeter, pixel
p = blade position
Po = impeller power number $\left(=\langle\varepsilon\rangle V/N^3D^5\right)$, (-)
r = radial position, m
$\mathbf{r}$ = position vector, m
R = impeller radius, m
S_{ij} = rate-of-strain tensor, s^{-1}
$\overline{S}_{ij}$ = rate-of-strain tensor for the resolved scale, s^{-1}
T = tank diameter, m
T_{ij} = compressible subgrid stress tensor, Pa
t_b = impeller blade thickness, m
$\overline{u}_i$ = filtered or solved instantaneous velocity (LES), m/s
u_i = instantaneous velocity, m/s
$\tilde{u}_i$ = periodic velocity, m/s
u'_i = fluctuating velocity, m/s
$\langle u_i^p \rangle$ = *phase*-averaged velocity for any blade position, m/s
$\overline{U}_i$ = i-th component of mean velocity, m/s
U_{tip} = tip velocity, m/s
V_i = volume of a computational cell, m^3
(r,t,ax) = radial, tangential and axial
(x,y,z) = Cartesian coordinate system

Greek Letters

γ = shear rate, s^{-1}
ε = dissipation rate of turbulent kinetic energy, m^2/s^3
$\langle\varepsilon\rangle$ = vessel-averaged energy dissipation rate, m^2/s^3
$\langle\varepsilon^p\rangle$ = phase-average dissipation rate for any blade position, m^2/s^3
ε^θ = phase-resolved energy dissipation rate, m^2/s^3
ε^{SGS} = subgrid-scale dissipation rate (LES), m^2/s^3
θ = phase angle from any impeller blade, degree
κ = von Karman constant
λ = Taylor microscale, m
μ = dynamic viscosity, Pa.s
μ_t = turbulent viscosity, Pa.s
ξ = dimensionless vorticity magnitude
$\langle\xi^p\rangle$ = phase-average vorticity magnitude for any blade position
ρ = liquid density, kg/m^3
σ_{ij} = molecular viscosity stress tensor (LES), Pa
$\boldsymbol{\tau}$ = stress tensor, Pa
τ_{max} = maximum hydrodynamic stress, Pa
τ_{ij} = subgrid turbulent stress tensor (LES), Pa
τ_{kk} = isotropic subgrid-scale stress tensor, Pa
ϕ = density-weighted (or Favre) filtering operator
ω = vorticity magnitude normal to plane, s^{-1}
$\boldsymbol{\Omega}$ = angular velocity vector, rps

Literature Cited

1. Elimelech M, Gregory J, Jia X, Williams RA. *Particle Deposition and Aggregation, Measurement, Modelling and Simulation*. Woburn: Butterworth-Heinemann; 1995.
2. Bäbler MU, Morbidelli M, Baldyga J. Modelling the breakage of solid aggregates in turbulent flows. *J Fluid Mech*. 2008;612:261–289.
3. Babler MU, Biferale L, Lanotte AS. Breakup of small aggregates driven by turbulent hydrodynamical stress. *Phys Rev E*. 2012;85(2).
4. Sonntag RC, Russel WB. Structure and breakup of flocs subjected to fluid stresses. I. Shear experiments. *J Colloid Interface Sci*. 1986; 113(2):399–413.
5. Sonntag RC, Russel WB. Structure and breakup of flocs subjected to fluid stresses III. Converging flow. *J Colloid Interface Sci*. 1987; 115:390–395.
6. Higashitani K, Inada N, Ochi T. Floc breakup along centerline of contractile flow to orifice. *Colloids Surf*. 1991;56:13–23.
7. Vassileva ND, van den Ende D, Mugele F, Mellema J. Fragmentation and erosion of two-dimensional aggregates in shear flow. *Langmuir*. 2007;23:2352–2361.
8. Soos M, Ehrl L, Bäbler MU, Morbidelli M. Aggregate breakup in a contracting nozzle. *Langmuir*. 2010;26:10–18.
9. Harshe YM, Lattuada M, Soos M. Experimental and modeling study of breakage and restructuring of open and dense colloidal aggregates. *Langmuir*. 2011;27(10):5739–5752.
10. Glasgow LA, Hsu JP. An experimental study of floc strength. *AIChE J*. 1982;28:779–785.
11. Spicer PT, Keller W, Pratsinis SE. The effect of impeller type on floc size and structure during shear-induced flocculation. *J Colloid Interface Sci*. 1996;184:112–122.
12. Kobayashi M, Adachi Y, Ooi S. Breakup of fractal flocs in a turbulent flow. *Langmuir*. 1999;15:4351–4356.
13. Blaser S. Flocs in shear and strain flows. *J. Colloid Interface Sci*. 2000;225:273–284.
14. Blaser S. Break-up of flocs in contraction and swirling flows. *Colloids Surf A*. 2000;166:215–223.
15. Coufort C, Bouyer D, Liné A. Flocculation related to local hydrodynamics in a Taylor-Couette reactor and in a jar. *Chem Eng Sci*. 2005;60:2179–2192.
16. Bouyer D, Coufort C, Liné A, Do-Quang Z. Experimental analysis of floc size distributions in a 1-L jar under different hydrodynamics and physicochemical conditions. *J Colloid Interface Sci*. 2005;292: 413–428.
17. Bouyer D, Liné A, Do-Quang Z. Experimental analysis of floc size distribution under different hydrodynamics in a mixed tank. *AIChE J*. 2004;50:2064–2081.
18. Soos M, Moussa A, Ehrl L, Sefcik J, Wu H, Morbidelli M. Effect of shear rate on aggregate size and morphology investigated under turbulent conditions in stirred tank. *J Colloid Interface Sci*. 2008;319 577–589.
19. Ehrl L, Soos M, Morbidelli M. Dependence of aggregate strength, structure, and light scattering properties on primary particle size under turbulent conditions in stirred tank. *Langmuir*. 2008;24:3070–3081.
20. Ehrl L, Soos M, Wu H, Morbidelli M. Effect of flow field heterogeneity in coagulators on aggregate size and structure. *AIChE J*. 2010; 56:2573–2587.
21. Sonntag RC, Russel WB. Structure and breakup of flocs subjected to fluid stresses. II. Theory. *J Colloid Interface Sci*. 1987;115(2):378–389.
22. Potanin AA. On the computer simulation of the deformation and breakup of colloidal aggregates in shear flow. *J Colloid Interface Sci*. 1993;157:399–410.
23. Higashitani K, Iimura K, Sanda H. Simulation of deformation and breakup of large aggregates in flows of viscous fluids. *Chem Eng Sci*. 2001;56:2927–2938.
24. Harada S, Tanaka R, Nogami H, Sawada M. Dependence of fragmentation behavior of colloidal aggregates on their fractal structure. *J Colloid Interface Sci*. 2006;301(1):123–129.
25. Harada S, Tanaka R, Nogmi H, Sawada M, Asakura K. Structural change in nonfractal particle clusters under fluid stress. *Colloids Surf A*. 2007;302(1-3):396–402.
26. Zaccone A, Soos M, Lattuada M, Wu H, Morbidelli M. Breakup of dense colloidal aggregates under hydrodynamic stresses. *Phys Rev E*. 2009;79:61401.
27. Eggersdorfer ML, Kadau D, Herrmann HJ, Pratsinis SE. Fragmentation and restructuring of soft-agglomerates under shear. *J Colloid Interface Sci*. 2010;342(2):261–268.
28. Harshe YM, Lattuada M. Breakage rate of colloidal aggregates in shear flow through stokesian dynamics. *Langmuir*. 2012;28(1):283–292.
29. Wu H, Patterson GK. Laser-Doppler measurements of turbulent-flow parameters in a stirred mixer. *Chem Eng Sci*. 1989;44(10):2207–2221.
30. Kresta SM, Wood PE. Prediction of the three-dimensional turbulent flow in stirred tank. *AIChE J*. 1991;37(3):448–460.
31. Micheletti M, Baldi S, Yeoh SL, et al. On spatial and temporal variations and estimates of energy dissipation in stirred reactors. *Chem Eng Res Des*. 2004;82(A9):1188–1198.
32. Ducci A, Yianneskis M. Direct determination of energy dissipation in stirred vessels with two-point LDA. *AIChE J*. 2005;51(8):2133–2149.
33. Sharp KV, Adrian RJ. PIV study of small scale flow structure around a Rushton turbine. *AIChE J*. 2001;47(4):766–778.

34. Escudié R, Liné A. Experimental analysis of hydrodynamics in a radially agitated tank. *AIChE J*. 2003;49:585–603.
35. Delafosse A, Collignon ML, Crine M, Toye D. Estimation of the turbulent kinetic energy dissipation rate from 2D-PIV measurements in a vessel stirred by an axial Mixel TTP impeller. *Chem Eng Sci*. 2011;66(8):1728–1737.
36. Feng H, Olsen MG, Liu Y, Fox FO, Hill JC. Investigation of turbulent mixing in a confined planar-jet reactor. *AIChE J*. 2005;51:2649–2664.
37. Costes J, Couderc JP. Study by laser doppler anemometry of the turbulent - Flow induced by a Rushton turbine in a stirred tank - influence of the size of the units. 2. Spectral analysis and scales of turbulence. *Chem Eng Sci*. 1988;43(10):2765–2772.
38. Zhou G, Kresta SM. Impact of tank geometry on the maximum turbulence energy dissipation rate for impellers. *AIChE J*. 1996;42(9):2476–2490.
39. Baldi S. *Energy Dissipation Measurements in Stirred Vessels with Particle Image Velocimetry* [PhD thesis]. London, UK, King's College London; 2004.
40. Wichterle K, Kadlec M, Zak L, Mitschka P. Shear rates on turbine impeller blades. *Chem Eng Com*. 1984;26(1-3):25–32.
41. Joshi JB, Nere NK, Rane CV, et al. CFD simulation of stirred tanks: Comparison of turbulence models, Part I: Radial flow impellers. *Can J Chem Eng*. 2011;89(1):23–82.
42. Derksen J, Van den Akker HEA. Large eddy simulations on the flow driven by a Rushton turbine. *AIChE J*. 1999;45(2):209–221.
43. Derksen JJ. The Lattice-Boltzmann method for multiphase fluid flow simulations and Euler-Lagrange Large-Eddy simulations. In: Marchisio DL, Fox RO, eds. *Multiphase Reacting Flows: Modelling and Simulation*. New York: Springer; 2007:181–228.
44. Derksen JJ, Kontomaris K, McLaughlin JB, Van den Akker HEA. Large-eddy simulation of single-phase flow dynamics and mixing in an industrial crystallizer. *Chem Eng Res Des*. 2007;85(A2):169–179.
45. Hartmann H, Derksen JJ, Montavon C, Pearson J, Hamill IS, van den Akker HEA. Assessment of large eddy and RANS stirred tank simulations by means of LDA. *Chem Eng Sci*. 2004;59(12):2419–2432.
46. Hartmann H, Derksen JJ, van den Akker HEA. Macroinstability uncovered in a Rushton turbine stirred tank by means of LES. *AIChE J*. 2004;50(10):2383–2393.
47. Hartmann H, Derksen JJ, van den Akker HEA. Mixing times in a turbulent stirred tank by means of LES. *AIChE J*. 2006;52(11):3696–3706.
48. Pascual MR, Ravelet F, Delfos R, Derksen JJ, Witkamp GJ. Large eddy simulations and stereoscopic particle image velocimetry measurements in a scraped heat exchanger crystallizer geometry. *Chem Eng Sci*. 2009;64(9):2127–2135.
49. van Vliet E, Derksen JJ, van den Akker HEA. Turbulent mixing in a tubular reactor: Assessment of an FDF/LES approach. *AIChE J*. 2005;51(3):725–739.
50. Yoon HS, Balachandar S, Ha MY, Kar K. Large Eddy simulation of flow in a stirred tank. *Trans ASME J Fluids Eng*. 2003;125(3):486–499.
51. Yeoh SL, Papadakis G, Yianneskis M. Numerical simulation of turbulent flow characteristics in a stirred vessel using the les and rans approaches with the sliding/deforming mesh methodology. *Chem Eng Res. Des*. 2004;82(A7):834–848.
52. Bakker A, Oshinowo LM. Modelling of turbulence in stirred vessels using large eddy simulation. *Chem Eng Res Des*. 2004;82(A9):1169–1178.
53. Alcamo R, Micale G, Grisafi F, Brucato A, Ciofalo M. Large-eddy simulation of turbulent flow in an unbaffled stirred tank driven by a Rushton turbine. *Chem Eng Sci*. 2005;60(8-9):2303–2316.
54. Delafosse A, Line A, Morchain J, Guiraud P. LES and URANS simulations of hydrodynamics in mixing tank: Comparison to PIV experiments. *Chem Eng Res Des*. 2008;86(12A):1322–1330.
55. Murthy BN, Joshi JB. Assessment of standard k-epsilon, RSM and LES turbulence models in a baffled stirred vessel agitated by various impeller designs. *Chem Eng Sci*. 2008;63(22):5468–5495.
56. Yoon HS, Balachandar S, Ha MY. Large eddy simulation of flow in an unbaffled stirred tank for different Reynolds numbers. *Phys Fluids*. 2009;21(8).
57. Pope SB. Turbulent flows. Cambridge: Cambridge University Press; 2000.
58. Smagorinsky J. General Circulation experiments with the primitive equations I. The basic experiment. *Mon Weather Rev*. 1963;91:99–164.
59. Lilly DK. *On the Application of the Eddy Viscosity Concept in the Internal Subrange of Turbulence*. Boulder, CO: National Center for Atmospheric Research; 1966.
60. Moussa AS, Soos M, Sefcik J, Morbidelli M. Effect of the solid volume fraction on the aggregation and breakage of colloidal suspensions in batch and continuous stirred tank. *Langmuir*. 2007;23:1664–1673.
61. Soos M, Moussa A, Ehrl L, Sefcik J, Wu H, Morbidelli M. Dynamic response studies of aggregation and breakage dynamics in colloidal dispersions in stirred tanks. *J Disper Sci Technol*. 2008;29:1–6.
62. Kerker M. The scattering of light. New York: Academic Press; 1969.
63. Jones AR. Lights scattering for particle characterization. *Prog Energ Combust*. 1999;25:1–53.
64. Mandelbrot BB, Passoja DE, Paullay AJ. Fractal character of fracture surfaces of metals. *Nature*. 1984;308:721–722.
65. Lee C, Kramer TA. Prediction of three-dimensional fractal dimension using the two-dimensional properties of fractal aggregates. *Adv Colloid Interface Sci*. 2004;112:49–57.
66. Ehrl L, Soos M, Lattuada M. Generation and geometrical analysis of dense clusters with variable fractal dimension. *J Phys Chem B*. 2009;113:10587–10599.
67. Delafosse A, Morchain J, Guiraud P, Line A. Trailing vortices generated by a Rushton turbine: assessment of URANS and large eddy simulations. *Chem Eng Res Des*. 2009;87(4):401–411.
68. Van't Riet K, Smith JM. The trailing vortex system produced by Rushton turbine agitators. *Chem Eng Sci*. 1975;30(9):1093–1105.
69. Yianneskis M, Popiolek Z, Withelaw JH. An experimental study of the steady and unsteady flow characteristics of stirred reactors. *J Fluid Mech*. 1987;175:537–555.
70. Stoots CM, Calabrese RV. Mean velocity-field relative to a Rushton turbine blade. *AIChE J*. 1995;41(1):1–11.
71. Lee KC, Yianneskis M. Turbulence properties of the impeller stream of a Rushton turbine. *AIChE J*. 1998;44:13–24.
72. Lu WM, Yang BS. Effect of blade pitch on the structure of the trailing vortex around Rushton turbine impellers. *Can J Chem Eng*. 1998;76(3):556–562.
73. Escudié R, Bouyer D, Liné A. Characterization of trailing vortices generated by a Rushton turbine. *AIChE J*. 2004;50:75–86.
74. Jeong J, Hussain F. On the indentification of a vortex. *J Fluid Mech*. 1995;285:69–94.
75. Campolo M, Sbrizzai F, Soldati A. Time-dependent flow structures and Lagrangian mixing in Rushton-impeller baffled-tank reactor. *Chem Eng Com*. 2003;58:1615–1629.
76. Rutherford K, Mahmoudi MS, Lee KC, Yianneskis M. The influence of Rushton impeller blade and disk thickness on the mixing characteristics of the stirred vessels. *Trans Inst Chem Eng*. 1996;74:369–378.
77. Nagata S. *Mixing, Principles ans Applications*. New York: John Wiley and Sons, Inc.; 1975.
78. Rushton JH, Costich EW, Everett HJ. Power characteristics of mixing impellers. *Chem Eng Prog*. 1950;46(8):395–476.
79. Distelhoff MFW, Laker J, Marquis AJ, Nouri JM. The application of a strain-gauge technique to the measurement of the power characteristics of five impellers. *Exp Fluids*. 1995;20:56–58.
80. Baldi S, Yianneskis M. On the quantification of energy dissipation in the impeller stream of a stirred vessel from fluctuating velocity gradient measurements. *Chem Eng Sci*. 2004;59:2659–2671.
81. Kusters KA. *The Influence of Turbulence on Aggregation of Small Particles in Agitated Vessel* [PhD thesis]. Eindhoven, Netherlands, Eindhoven University of Technology; 1991.
82. Kusters KA, Wijers JG, Thoenes D. Aggregation kinetics of small particles in agitated vessels. *Chem Eng Sci*. 1997;52(1):107–121.
83. Zhou GW, Kresta SM. Correlation of mean drop size and minimum drop size with the turbulence energy dissipation and the flow in an agitated tank. *Chem Eng Sci*. 1998;53(11):2063–2079.
84. Peter C, Suzuki Y, Buchs J. Hydromechanical stress in shake flasks: Correlation for the maximum local energy dissipate rate. *Biotech Bioeng*. 2006;93(6):1164–1176.

Manuscript received Apr. 8, 2013, and revision received Jun. 28, 2013.